RSC Advances

This is an *Accepted Manuscript*, which has been through the Royal Society of Chemistry peer review process and has been accepted for publication.

Accepted Manuscripts are published online shortly after acceptance, before technical editing, formatting and proof reading. Using this free service, authors can make their results available to the community, in citable form, before we publish the edited article. This *Accepted Manuscript* will be replaced by the edited, formatted and paginated article as soon as this is available.

You can find more information about *Accepted Manuscripts* in the Information for Authors.

Please note that technical editing may introduce minor changes to the text and/or graphics, which may alter content. The journal's standard Terms & Conditions and the Ethical guidelines still apply. In no event shall the Royal Society of Chemistry be held responsible for any errors or omissions in this *Accepted Manuscript* or any consequences arising from the use of any information it contains.

ROYAL SOCIETY OF CHEMISTRY

www.rsc.org/advances

Facile Synthesis and Enhanced Visible-Light Photocatalytic Activity of Graphitic Carbon Nitride Decorated with Ultrafine Fe_2O_3 Nanoparticles

Xin Liu,[1] Ailing Jin,[1] Yushuai Jia,* Junzhe Jiang, Na Hu, and Xiangshu Chen

[*] Corresponding author: Dr. Yushuai Jia

Email: ysjia@jxnu.edu.cn (Y. S. Jia)

[1] The authors contribute equally to this work.

Jiangxi Inorganic Membrane Materials Engineering Research Centre, College of Chemistry and Chemical Engineering, Jiangxi Normal University, Nanchang 330022, P. R. China

Abstract: Hybrid nanocomposites based on graphitic carbon nitride (g-C_3N_4) nanosheets supported ultrafine Fe_2O_3 nanoparticles have been successfully prepared by a facile thermal polymerization and deposition-precipitation method. Characterization results demonstrate that Fe_2O_3/g-C_3N_4 nanocomposites exhibit a well-defined morphology, in which Fe_2O_3 nanocrystals of 3 nm size with a narrow particle distribution are uniformly dispersed on the layers of the g-C_3N_4 nanosheets. Photocatalytic reaction results indicate that the photocatalytic activity of g-C_3N_4 is significantly enhanced after introduction of a small amount of Fe_2O_3, and the optimum activity of the Fe_2O_3/g-C_3N_4 nanocomposites with a weight ratio of Fe_2O_3 at 0.1% is up to about 3 times and 62 times as high as that of pure g-C_3N_4 and pure Fe_2O_3, respectively, for the degradation of organic dye Rhodamine B (RhB) under visible light irradiation. The high performance of the Fe_2O_3/g-C_3N_4 photocatalysts is mainly attributed to the synergistic effect at the interface of heterojunction between Fe_2O_3 nanoparticles and g-C_3N_4 nanosheets, including improved separation efficiency of the charge carriers, the suppressed recombination process and the suitable band position of the composites. These results underline the potential for the development of effective, low-cost and earth-abundant photocatalysts for the promotion of water splitting and environment remediation under natural sunlight by construction sustainable g-C_3N_4 polymer materials.

Keywords: Photocatalysis, Graphitic carbon nitride, Fe_2O_3 nanoparticles, High dispersion, Visible light

RSC Advances Accepted Manuscript

1. Introduction

In view of current increasing crisis of energy shortage and environmental problems, semiconductor-based photocatalysis technology has attracted considerable attention due to its extensive applications in hydrogen generation from water splitting,[1-2] degradation of environmental pollutants,[3] CO_2 reduction,[4] selective organic synthesis[5] and air purification.[6] At present, developing of efficient, inexpensive, non-toxic and stable materials as photocatalysts capable of harvesting solar light in the visible region still remains a great challenge in this field.[1-2,7-8] Recently, a novel polymeric semiconductor, graphitic carbon nitride (g-C_3N_4) was firstly reported by Wang et al.[9] as a metal-free photocatalyst for visible-light photocatalytic water splitting. Moreover, because of its simple fabrication, low-cost, high chemical and thermal stability, suitable band gap and tunable electronic structure, g-C_3N_4 is considered to be a very promising photocatalyst for various potential applications.[10-13] However, the low separation efficiency and high recombination rate of photogenerated electrons and holes greatly restrict the photocatalytic activity of pure g-C_3N_4 for practical use. In addition, the band gap of g-C_3N_4 is still as large as 2.7 eV, corresponding to an optical wavelength just at 450 nm, which also seriously limits its visible-light response and photocatalytic performance.

To enhance the visible-light photocatalytic activity of g-C_3N_4, a variety of methods have been developed, including metal and nonmetal doping,[6,14-17] nanostructure designing,[18-19] sensitizing with organic dyes[20-21] and coupling with other semiconductors to form composite photocatalysts.[22-27] Among these strategies, semiconductor combination is one of the most effective and convenient methods for improving the photocatalytic performance with a formation of a heterojunction structure. Ge et al.[28] reported a CdS quantum dots coupled g-C_3N_4 photocatalyst with a hydrogen evolution rate 9 times that of pure g-C_3N_4 owing to the synergistic effect of the heterostructure. He et al.[23] prepared SnO_{2-x}/g-C_3N_4 composite photocatalyst via a calcination process and suggested that the enhanced RhB photodegradation activity benefited from a direct Z-scheme mechanism, which promoted light absorption and the separation of charge carriers. Huang et al.[29] developed WO_3/g-C_3N_4 heterojuncion photocatalyst by a calcination method that showed much higher efficiency for

RSC Advances Accepted Manuscript

the photodegradation of organic pollutants than that of pure samples.

As a promising candidate photocatalyst, Fe_2O_3 is a typical non-toxic semiconductor with a narrow band gap of about 2.2 eV (much smaller than that of g-C_3N_4), which can absorb light up to 600 nm, corresponding to approximately 40% of the solar spectrum energy. Besides, the superior properties of good chemical stability, high electrical conductivity, earth abundance and low cost make Fe_2O_3 advantageous over other semiconductor materials.[30] However, the photocatalytic activity of Fe_2O_3 is rather low due to high electron-hole recombination rate. It has been reported that fabrication of nanosized Fe_2O_3 particles could largely enhance the photocatalytic performance of this material.[31-32] Therefore, it is then expected that if g-C_3N_4 was combined with Fe_2O_3 nanoparticles of high dispersion to form heterojunction nanocomposites, some intrinsic disadvantages of g-C_3N_4 such as the low separation efficiency of charge carriers and the limited visible-light absorption ability can be well overcome and it can be highly possible to achieve excellent photocatalytic activity under visible light irradiation.

Up to now, for synthesizing composites of g-C_3N_4 coupled with another semiconductor, most of the preparation processes employed conventional calcination or hydrothermal methods by simply combining the mixture of two pure samples or precursors together, while the direct and controllable growth of highly dispersed semiconductor nanoparticles on the layers of g-C_3N_4 has been rarely exploited, and the relationship between well-defined structure and photocatalytic performance needs to be further clarified. Ye et al.[25] synthesized Fe_2O_3/g-C_3N_4 photocatalyst by calcination two precursors ($FeCl_3 \cdot 6H_2O$ and melamine) at 520°C. Theerthagiri et al.[26] mixed the two pure composites (Fe_2O_3 and g-C_3N_4) and sintered them at 300°C to synthesize Fe_2O_3/g-C_3N_4 hybrid. In this work, we report a well-defined Fe_2O_3/g-C_3N_4 nanocomposite for the photocatalytic degradation of organic pollutant Rhodamine B (RhB) under visible light illumination. A facile strategy via a deposition-precipitation method has been developed and Fe_2O_3 nanoparticles with a diameter of 3 nm are homogeneously deposited on g-C_3N_4 nanosheets. Our results reveal that the photocatalytic activity of g-C_3N_4 is significantly improved after introduction of Fe_2O_3 nanoparticles and the optimum photocatalytic activity of Fe_2O_3/g-C_3N_4 composites is achieved at a weight ratio of 0.1% Fe_2O_3. XRD, SEM, high-resolution TEM, XPS, DRS and

RSC Advances Accepted Manuscript

PL spectra are employed to analyze the origin of the superior photocatalytic performance and a possible mechanism is proposed.

2. Experimental section

2.1 Preparation of photocatalysts

Urea and Ferric nitrate nonahydrate (analytical grade purity) were purchased from Sinopharm Chemical Reagent Co., Ltd. and were used without further purification. All other reagents used in this work were of analytical grade and were used as received.

Metal-free g-C_3N_4 nanosheets were prepared by a thermal polymerization method. In a typical synthesis, urea was loaded into an alumina crucible with a lid and heated in a muffle furnace at a ramping rate of 5°C/min to 550°C. This temperature was held for 4 h prior to cooling to room temperature naturally. The yellow product was collected and ground into a fine powder.

Fe_2O_3/g-C_3N_4 nanocomposites were synthesized using a facile deposition-precipitation method. As illustrated in Fig. 1, 200 mg g-C_3N_4 powder was first dispersed in 50 ml water by ultrasonication for 30 min. Then the mixture was transferred into a water-bath and continuously stirred at 70°C, followed by adding of 10 ml $Fe(NO_3)_3$—ethanol solution (calculated amount of $Fe(NO_3)_3 \cdot 9H_2O$ dissolved in ethanol) dropwise. After that, the pH value of the mixture was adjusted to 8 by careful adding of 10% ammonium hydroxide. Subsequently, the obtained solid after evaporation of the solvent was gradually heated to 400°C in Ar atmosphere and kept for 3 h to reach complete decomposition of Fe precursors. The final composite Fe_2O_3/g-C_3N_4 photocatalysts with various Fe_2O_3 content (0.05 wt%, 0.1 wt%, 0.3 wt%, 0.6 wt% and 1 wt%) were obtained. For comparison, pure Fe_2O_3 nanopowder was also prepared following the above-mentioned procedure in the absence of g-C_3N_4.

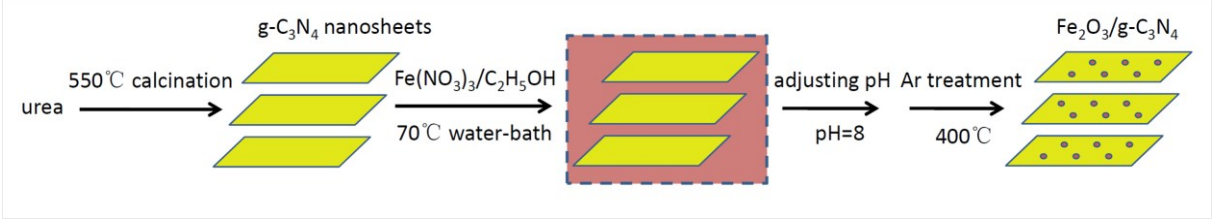

Fig. 1 Schematic diagram of the preparation process of Fe_2O_3/g-C_3N_4 nanocomposites.

RSC Advances Accepted Manuscript

2.2 Characterization of photocatalysts

X-ray diffraction (XRD) was performed on a Rigaku RINT-2200 diffractometer using Cu Kα radiation source at 40 kV and 20 mA. The morphologies and microstructures of the samples were investigated by scanning electron microscopy (SEM) on a Hitachi SU-8020 cold field emission instrument and by high resolution transmission electron microscopy (HRTEM) run on a JEOL JEM-2100 microscope at 200 kV. Energy-dispersive X-ray (EDX) spectroscopy attached to SEM was used to determine the chemical composition of the composite. X-ray photoelectron spectroscopy (XPS) was measured on a VG-ESCALAB 250Xi instrument with a monochromatic Al Kα source. The UV-vis diffuse reflectance spectra (DRS) were recorded on a JASCO V-750 instrument equipped with an integrating sphere in the range of 200−800 nm. The photoluminescence (PL) spectra were obtained at room temperature by an Edinburgh Instruments FLS980 Fluorescence Spectrometer with an excitation wavelength of 325 nm.

2.3 Photocatalytic reaction

The photocatalytic activities of the synthesized samples were evaluated by the degradation of Rhodamine B (RhB) under visible light irradiation. Typically, 0.03 g of the photocatalyst was dispersed into 200 ml of 20 mg L^{-1} aqueous solution of RhB via ultrasonic treatment for 10 min. Prior to irradiation, the suspension was magnetically stirred in the dark for an hour to establish the adsorption-desorption equilibrium of RhB onto the catalyst surface at room temperature. A 300 W Xe lamp with a UV cutoff filter ($\lambda > 400$ nm) was used as the light source to provide the visible light. At regular intervals, 4 ml of the suspension was withdrawn and centrifuged to remove the catalyst particles for analysis. The degradation of RhB was monitored by a UV-vis spectrophotometer (Hitachi, U-3310) by measuring its absorbance at 553 nm.

3. Results and discussion

3.1 Catalyst characterization

The XRD patterns of Fe_2O_3/g-C_3N_4 nanocomposites are shown in Fig. 2a, together with that of pure g-C_3N_4 and Fe_2O_3 nanopowder for comparison. Fe_2O_3 nanopowder exhibits diffraction peaks at 2θ 24.1, 33.1, 35.6, 40.9, 49.5, 54.1, 62.4, 64.0°, which are indexed to the

RSC Advances Accepted Manuscript

(012), (104), (110), (113), (024), (116), (214) and (300) planes of hematite α-Fe_2O_3 (JCPDS 33-0664), respectively. For pure g-C_3N_4 and Fe_2O_3/g-C_3N_4 composites, two broad peaks at 2θ 13.1 and 27.4° are observed, corresponding to the (100) and (002) crystal planes of g-C_3N_4, which are ascribed to the in-planar repeat period of the tri-s-triazine units and the interlayer spacing between graphitic layers, respectively.[9] However, no significant peaks for Fe_2O_3 can be detected in the Fe_2O_3/g-C_3N_4 patterns, probably due to the relatively low content of Fe_2O_3 in the composite ($\leqslant$1 wt%) and high dispersion of Fe_2O_3 nanoparticles on the g-C_3N_4. To get the XRD information of Fe species in the composite, we have added more Fe_2O_3 onto the g-C_3N_4 (20 wt%). It is found that obvious diffraction peaks of hematite α-Fe_2O_3 show up, which demonstrates the existence of Fe_2O_3 in the composite in the form of α-phase (Electronic Supplementary Information Fig. S1). The energy-dispersive X-ray (EDX) spectrum was used to analyze the chemical composition of the Fe_2O_3/g-C_3N_4 nanocomposite. As shown in Fig. 2b, the composite was composed of Fe, O, C, N and Si, among which the Si signal was from silicon foil used as SEM support for the powder sample, indicating that Fe_2O_3 was indeed loaded onto g-C_3N_4 nanosheets.

(a)

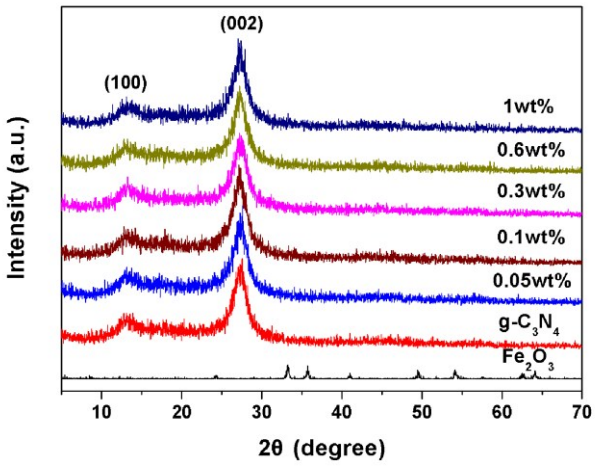

(b)

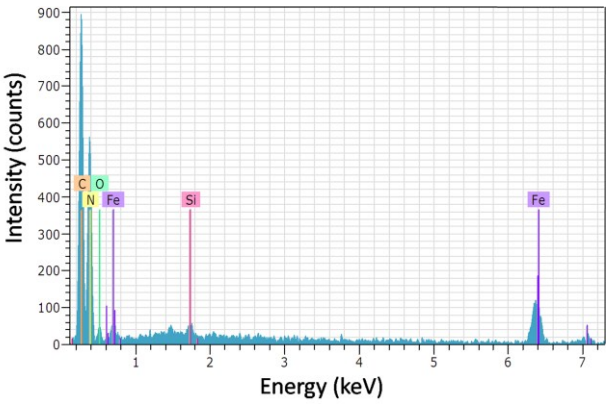

RSC Advances Accepted Manuscript

Fig. 2 (a) XRD patterns of Fe_2O_3/g-C_3N_4 nanocomposites with different Fe_2O_3 weight percentage; (b) EDX analysis of 1 wt% Fe_2O_3/g-C_3N_4.

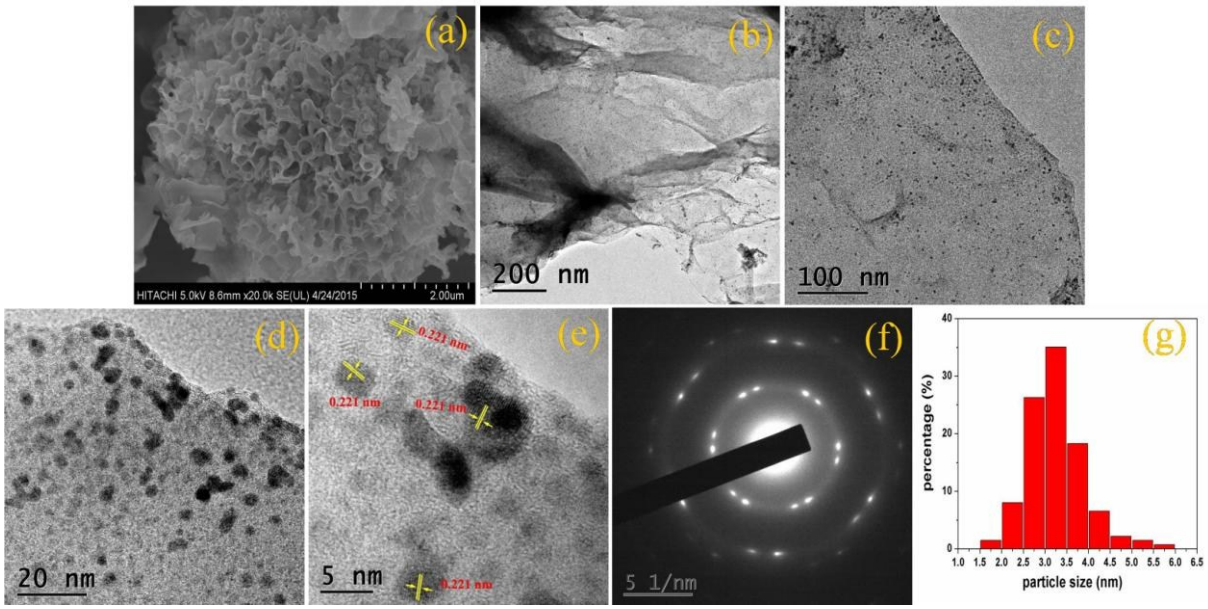

Fig. 3 FESEM image of pure g-C_3N_4 (a); TEM images (b-d), HRTEM image (e), SAED pattern (f) and particle size distribution (g) of 1 wt% Fe_2O_3/g-C_3N_4 nanocomposite.

The SEM image of pure g-C_3N_4 is shown in Fig. 3a. It can be seen that pure g-C_3N_4 prepared from urea by high temperature calcination presents flowerlike structure, which is composed of thin graphitic nanosheets with imbedded open nanopores of tens to several hundred nanometers diameter. The pure g-C_3N_4 of high porosity contributes to a large surface area of 38.9 m^2 g^{-1}, as determined by BET nitrogen adsorption/desorption isotherm (Electronic Supplementary Information Fig. S2). A high surface area means exposure of more active sites for g-C_3N_4 in the photocatalytic reaction. Fig. 3b-d exhibit typical TEM images of 1 wt% Fe_2O_3/g-C_3N_4 nanocomposite. As can be seen, ultrafine Fe_2O_3 nanoparticles are uniformly dispersed on the nanosheets of g-C_3N_4, with close contact between each other via forming some chemical bonds. This tight interaction is favorable for the formation of a heterojunction structure in the composites and promotes effective charge transfer and separation.[23] The d-spacing determined from HRTEM shown in Fig. 3e is 0.221 nm, corresponding to the (113) plane of hematite α-Fe_2O_3. To further confirm the microstructure of the composite, selected-area electron diffraction (SAED) was carried out on the area shown

RSC Advances Accepted Manuscript

in Fig. 3d. The SAED exhibits concentric diffraction rings, indicating that the dispersed Fe_2O_3 nanoparticles are polycrystalline and well crystallized (Fig. 3f). The particle size distribution of Fe_2O_3 nanocrystals is presented in Fig. 3g. By measuring more than 300 particles from HRTEM images, it is found that Fe_2O_3 particles have a narrow size distribution, with most of them falling in the range of 2.5—4.0 nm with a mean size of approximately 3 nm. The above results demonstrate that Fe_2O_3/g-C_3N_4 hybrid composites with well-defined structure have been successfully prepared by the facile deposition-precipitation method used in our work, which may have promising application in the photocatalytic reaction.

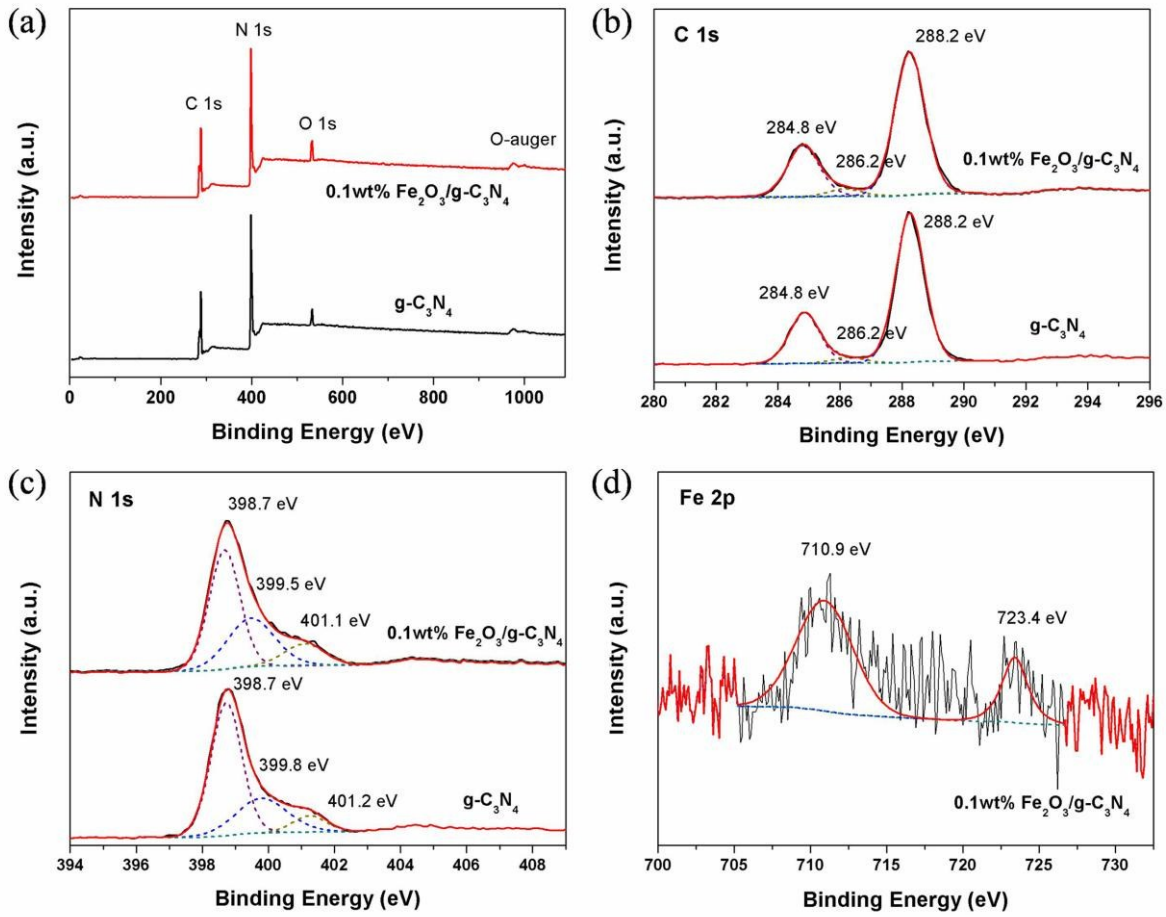

Fig. 4 XPS of synthesized g-C_3N_4 and 0.1 wt% Fe_2O_3/g-C_3N_4 nanocomposite: (a) survey spectra, (b) C 1s spectra, (c) N 1s spectra and (d) Fe 2p spectrum.

XPS measurements were carried out to investigate the chemical states of the surface composition in pure g-C_3N_4 and 0.1 wt% Fe_2O_3/g-C_3N_4 nanocomposite. Fig. 4a shows the survey scan XPS spectra of both samples. The strong peaks of C 1s, N 1s and O 1s are

RSC Advances Accepted Manuscript

observed in Fig. 4a, indicating the presence of C, N and O elements in both samples. While for 0.1 wt% Fe_2O_3/g-C_3N_4 sample, the Fe 2p signal is negligible, owing to the low content of Fe_2O_3 in the composite. High resolution spectra of C 1s, N 1s and Fe 2p are shown in Fig. 4b-d. As illustrated in Fig. 4b, three binding energy values of C 1s are observed at 284.8, 286.2 and 288.2 eV for both samples, which are assigned to sp^2 C-C bonds from carbon-containing contaminations, sp^3 hybridized carbon from the defects of g-C_3N_4 surface and sp^2-bonded carbon of N−C=N in the graphitic structure, respectively, with the latter constituting the major carbon composition in the g-C_3N_4.[33-35] In the N 1s spectrum of g-C_3N_4 (Fig. 4c), three peaks at 398.7, 399.8 and 401.2 eV can be clearly resolved, corresponding to sp^2 hybridized nitrogen (C−N=C), sp^3 hybridized nitrogen (H−N−$(C)_3$) and amino functional groups (C−NH_x), respectively.[17,34,36] However, two N 1s core levels of 0.1 wt% Fe_2O_3/g-C_3N_4 are found to be slightly shifted to lower binding energies (399.5 and 401.1 eV) compared with that of g-C_3N_4. This is probably due to the strong interaction between Fe_2O_3 and g-C_3N_4 in the heterostructure, which gives rise to charge transfer between each other.[37] The atomic ratio of C/N determined by the quantitative analysis results of XPS is 0.80 (the contribution of adventitious C 1s signal at 284.8 eV was deducted from the total C 1s peak area), which is close to the expected value of C/N in ideal g-C_3N_4 (0.75), reflecting the high graphitization degree of the g-C_3N_4 used in our experiments. The Fe 2p spectrum of 0.1 wt% Fe_2O_3/g-C_3N_4 (Fig. 4d) exhibits two characteristic peaks at 710.9 and 723.4 eV, attributed to typical Fe $2p_{3/2}$ and Fe $2p_{1/2}$ signals of Fe_2O_3 phase according to the literatures.[38-39] Therefore, the XPS results are in good agreement with the results of XRD and TEM that ultrafine Fe_2O_3 nanoparticles are evenly distributed on g-C_3N_4 nanosheets and thus heterostructures with close interconnection are formed.

To investigate the optical absorption properties of the as-prepared catalysts, we examined UV-vis diffuse reflectance spectra (DRS) of pure g-C_3N_4 and Fe_2O_3/g-C_3N_4 composites. As can be seen in Fig. 5, the g-C_3N_4 nanosheets show a strong absorption edge at about 450 nm, corresponding to the band gap of approximately 2.7 eV.[9,29,35] Compared to g-C_3N_4, all of the Fe_2O_3/g-C_3N_4 composites display similar visible light absorbance property but exhibit some red-shifts in absorption wavelength, and the absorption edge gradually moves towards longer wavelength as the Fe_2O_3 loading increases (the color of the composites evolves from yellow

RSC Advances Accepted Manuscript

to light brick-red), implying the strong interaction between Fe_2O_3 and g-C_3N_4 in the heterojunction structure, which results in modifications of optical properties of Fe_2O_3/g-C_3N_4 composites.[23]

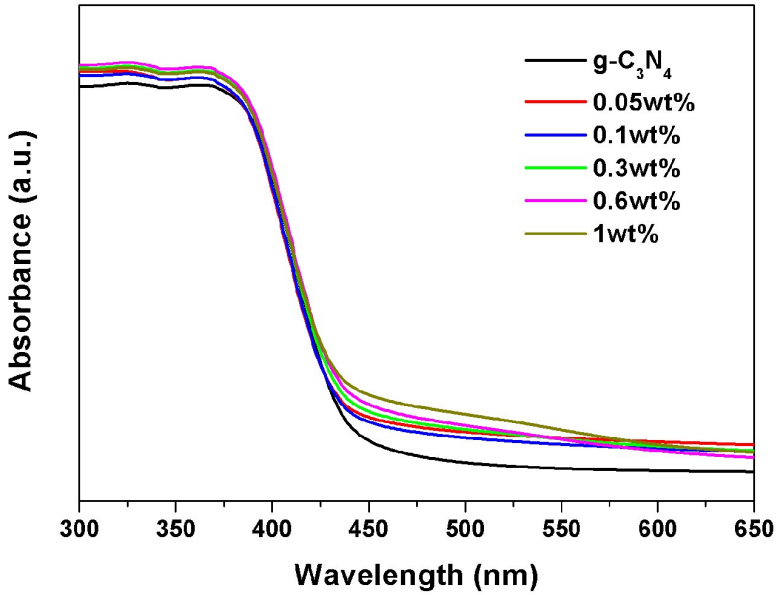

Fig. 5 UV-vis diffuse reflectance spectra of Fe_2O_3/g-C_3N_4 nanocomposites and pure g-C_3N_4.

3.2 Photocatalytic performance

RhB photodegradation was used to evaluate the photocatalytic activity of Fe_2O_3/g-C_3N_4 nanocomposite under visible light irradiation. Fig. 6 represents a comparison of spectral changes during the photocatalytic degradation of RhB over g-C_3N_4 and 0.1 wt% Fe_2O_3/g-C_3N_4 composite. For pure g-C_3N_4 (Fig. 6a), the photocatalytic degradation rate of RhB is quite slow and about 50% of the starting RhB molecules still remains after 90 min of the reaction time. However, it is evident from Fig. 6b that the intensity of the absorbance peak of RhB at 553 nm decreases rapidly within 90 min, indicating the superior photocatalytic activity for 0.1 wt% Fe_2O_3/g-C_3N_4. Thus, 0.1 wt% Fe_2O_3/g-C_3N_4 composite exhibits a much better photocatalytic performance than that of pure g-C_3N_4 nanosheets under the same conditions.

RSC Advances Accepted Manuscript

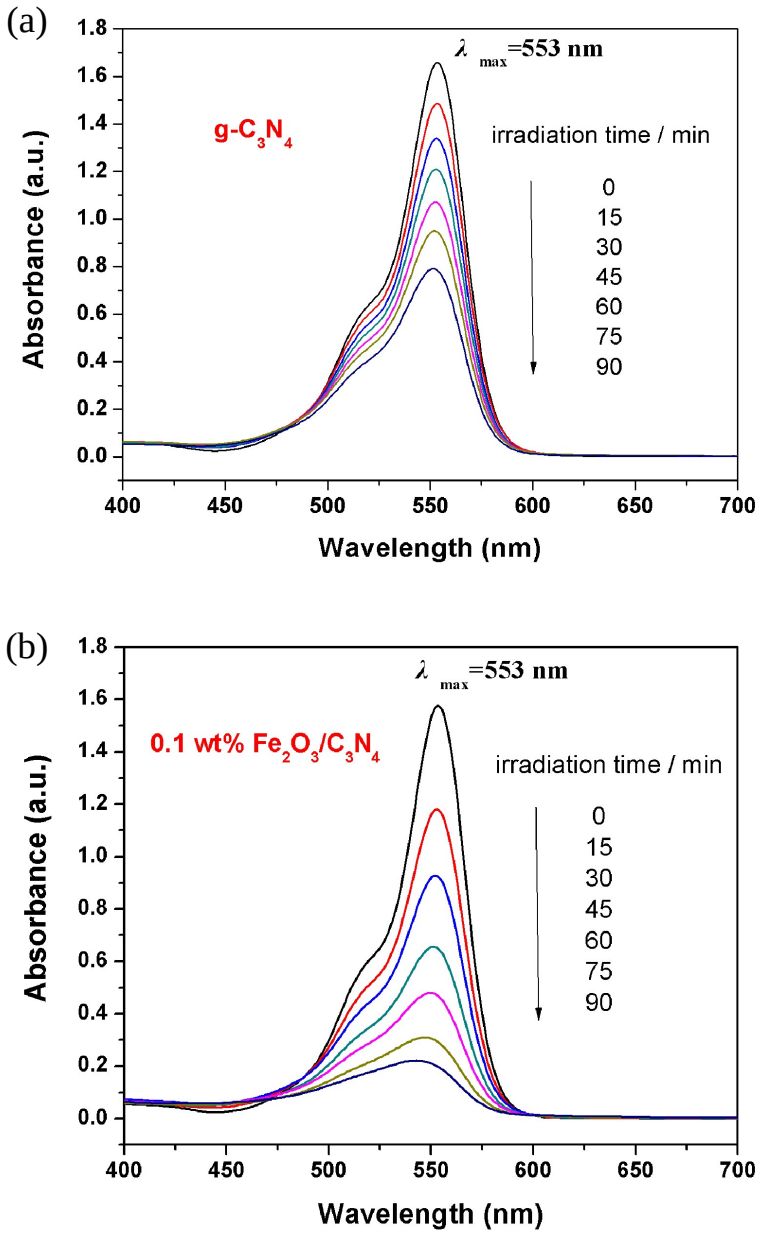

Fig. 6 Changes in UV-vis absorption spectra of RhB by (a) pure g-C_3N_4 and (b) 0.1 wt% Fe_2O_3/g-C_3N_4 nanocomposite under visible light irradiation.

RSC Advances Accepted Manuscript

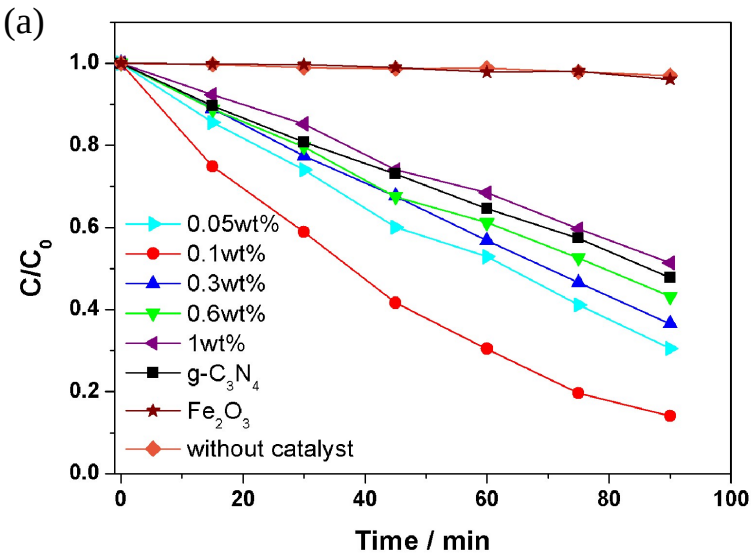

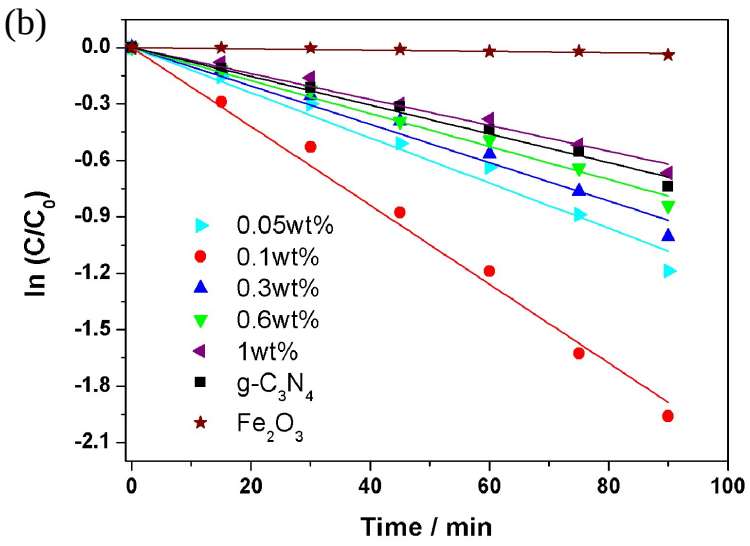

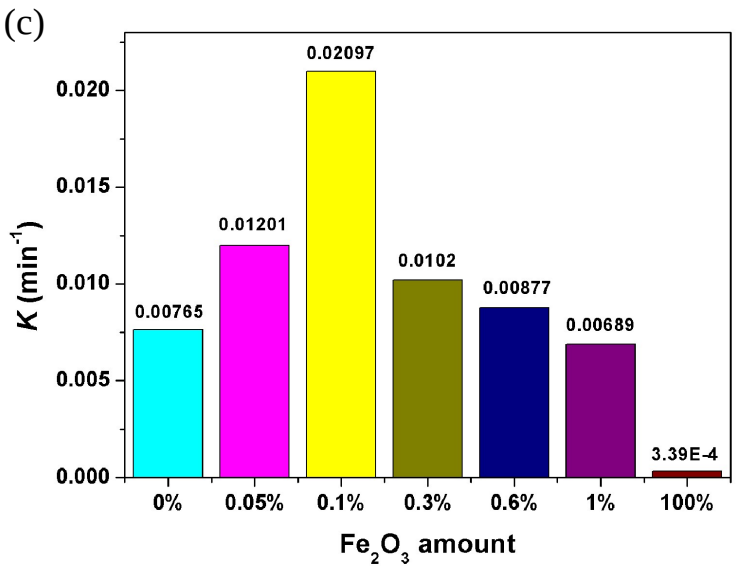

RSC Advances Accepted Manuscript

Fig. 7 (a) Photocatalytic activity, (b) first-order kinetics plot and (c) the kinetic constants for the degradation of RhB by g-C_3N_4, Fe_2O_3 nanopowder, and Fe_2O_3/g-C_3N_4 nanocomposite photocatalysts under visible light irradiation.

The detailed photocatalytic degradation activities for Fe_2O_3/g-C_3N_4 nanocomposites with various Fe_2O_3 content were further investigated and shown in Fig. 7a together with that of pure Fe_2O_3 nanopowder and g-C_3N_4 for comparison. A control experiment in the absence of a photocatalyst was also carried out, and it is observed that RhB self-degradation is almost negligible. No obvious degradation is observed with Fe_2O_3 nanopowder alone. For pure g-C_3N_4, only 50% of RhB has been degraded under visible light after irradiation for 90 min. With regard to the degradation of RhB over Fe_2O_3/g-C_3N_4 composites, the case is quite different. It is found that the Fe_2O_3 content has a great influence on the photocatalytic activities of g-C_3N_4, which is significantly enhanced after loading a very low amount of Fe_2O_3 nanoparticles (lower than 1 wt%). The photocatalytic activity first increases as the Fe_2O_3 content increases from 0.05 wt% to 0.1 wt%, and then decreases at a higher Fe_2O_3 content. When further increasing the loading of Fe_2O_3 higher than 1 wt% leads to activity lower than g-C_3N_4. These results suggest the existence of the synergistic effect of Fe_2O_3/g-C_3N_4 heterojunction, which can effectively improve the photocatalytic activity of Fe_2O_3/g-C_3N_4 composite via facilitated separation of charge carriers on the heterojunction interface. However, it should be noted that excess Fe_2O_3 species are detrimental to RhB degradation, which may be related to the recombination property of Fe_2O_3, more Fe_2O_3 greatly reducing the separation efficiency of photogenerated carriers and consequently lowering the photocatalytic activity of Fe_2O_3/g-C_3N_4. As a result, the optimum photocatalytic activity is achieved for the catalyst of 0.1 wt% Fe_2O_3/g-C_3N_4 composite (about 90% of RhB has been photodegraded within 90 min).

The experimental data in Fig. 7a can be well fit to a pseudo first-order kinetics equation

$$-\ln(C/C_0) = kt \qquad (1)$$

where k is the apparent first-order rate constant (min^{-1}), C and C_0 are the RhB concentration at reaction time t and 0, respectively. Fig. 7b shows the kinetics plot of Fe_2O_3/g-C_3N_4 nanocomposites for RhB photodegradation reaction. Upon varying the Fe_2O_3 content, the plot

RSC Advances Accepted Manuscript

of ln(C/C_0) against the irradiation time (t) is nearly a straight line, in which the slope of the fitting line is equal to the value of rate constant. The corresponding kinetic constants with different Fe_2O_3 content are shown in Fig. 7c. Even though we used less amount of catalyst and higher concentration of RhB in this reaction, the photocatalytic activities of Fe_2O_3/g-C_3N_4 composites have been already obviously better or comparable to that of some previously reported similar materials, and their preparation methods are much more complicated.[17,25-26] The highest apparent rate constant under our experimental conditions is determined to be 0.02097 min^{-1} for 0.1 wt% Fe_2O_3/g-C_3N_4 composite, which is about 3 times and 62 times higher than that of pure g-C_3N_4 (0.00765 min^{-1}) and pure Fe_2O_3 (3.39 E-4 min^{-1}), respectively, revealing the superior photocatalytic activity for highly dispersed Fe_2O_3/g-C_3N_4 composite materials.

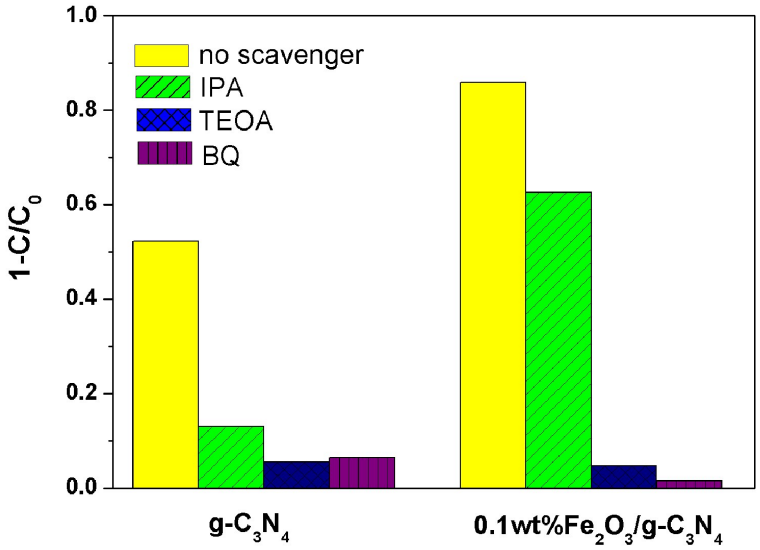

Fig. 8 Influences of various hole and radical scavengers in the system of photocatalytic degradation of RhB by pure g-C_3N_4 and 0.1 wt% Fe_2O_3/g-C_3N_4 under visible light irradiation for 90 min.

3.3 Proposed photocatalytic mechanism

The significantly enhanced photocatalytic activity of the hybrid composite catalysts motivates us to further study the photocatalytic reaction mechanism of the degradation process. Generally, photoinduced holes (h^+), hydroxyl radicals ($\dot{O}H$) and superoxide radicals ($\dot{O}_2^-$) are known to be the main reactive species involved in the photodegradation reaction.[20]

RSC Advances Accepted Manuscript

In our radical trapping experiments, 1 mmol/L of isopropanol (IPA), 1,4-benzoquinone (BQ) and triethanolamine (TEOA) were added into the solution and used as the hydroxyl radical, superoxide radical and hole scavengers, respectively, and their influences on the photocatalytic degradation efficiency for RhB are shown in Fig. 8. For both pure g-C_3N_4 and 0.1 wt% Fe_2O_3/g-C_3N_4, the photocatalytic degradation activities for RhB decrease remarkably by the adding of BQ and TEOA. However, when IPA is added, the activity is also declined, but not as significant as that with BQ and TEOA added. These results suggest that, under visible light irradiation, g-C_3N_4 and Fe_2O_3/g-C_3N_4 nanocomposite follow the similar photocatalytic mechanism for the degradation of RhB, in which the holes and superoxide radicals play a more important role than hydroxyl radicals. Thus, both holes and superoxide radicals are the primary active species in this reaction, which is consistent with previous reports.[20,40-41] Moreover, compared with g-C_3N_4, the photodegradation efficiency of Fe_2O_3/g-C_3N_4 sample declines more significantly with the same addition of BQ and TEOA, indicating that there may exist more superoxide radicals and holes in Fe_2O_3/g-C_3N_4 system than in g-C_3N_4 system due to the effective separation of photogenerated carriers.

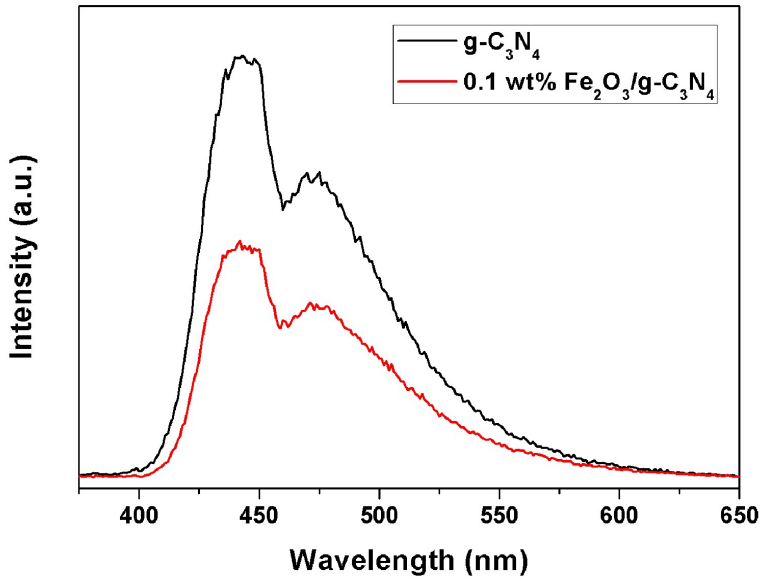

Fig. 9 Photoluminescence emission spectra of as-prepared pure g-C_3N_4 and 0.1 wt% Fe_2O_3/g-C_3N_4 samples.

The lifetime of charge carriers is of great importance to the performance of a photocatalytic

RSC Advances Accepted Manuscript

reaction. The formation of heterojunction structures in the composite photocatalysts may lead to the fast separation of electrons and holes and thus result in the high photodegradation activity. As is well known that the photoluminescence (PL) emission spectra mainly stem from the recombination of free charge carriers in semiconductors,[42] we carried out the room-temperature photoluminescence studies on the as-prepared samples to investigate the migration and separation efficiency of photogenerated electron-hole pairs. Fig. 9 represents the comparison of PL spectra for pure g-C_3N_4 and 0.1 wt% Fe_2O_3/g-C_3N_4 with an excitation wavelength of 325 nm. As for pure g-C_3N_4, a strong emission peak at about 445 nm and a shoulder peak around 475 nm are observed. After hybridization with Fe_2O_3 nanoparticles, the overall intensity of PL signals shows an obvious decrease, indicating that the recombination rate of photoinduced electron-hole pairs is greatly suppressed, which lengthens the lifetime of photogenerated carriers and subsequently favors the enhancement of photocatalytic performance.[23,43] Therefore, it can be deduced from Fig. 9 that the higher photocatalytic activity for Fe_2O_3/g-C_3N_4 compared with pure g-C_3N_4 may arise from the higher separation efficiency of electron-hole pairs.

Based on above experimental results, a possible mechanism has been proposed for the enhanced visible-light activity of Fe_2O_3/g-C_3N_4 composite catalysts and a schematic diagram is illustrated in Fig. 10. The significant improvement of photocatalytic performance can be ascribed to the synergistic effect between Fe_2O_3 nanocrystals and g-C_3N_4 nanosheets. The band gaps of Fe_2O_3 and g-C_3N_4 are 2.2 eV[44] and 2.7 eV[9], respectively, so both pure samples can be excited by visible light and produce photoinduced electrons and holes. After Fe_2O_3 nanoparticles are dispersed on g-C_3N_4 nanosheets, the two types of semiconductors closely combine together and form heterojunction interface. Since both the bottom of the conduction band (CB) and the top of the valence band (VB) of g-C_3N_4 (-1.3 V and 1.4 V vs. NHE, pH=7)[45-46] are more negative than that of Fe_2O_3 (0.28 V and 2.48 V vs. NHE, pH=7)[44], the photogenerated electrons could transfer easily from g-C_3N_4 into the CB of Fe_2O_3, while the holes could migrate from Fe_2O_3 into the VB of g-C_3N_4 via the interface of the heterojunction. As a result, the redistribution of electrons and holes on each side of the heterojunction is achieved (as shown in Fig. 10), which greatly hinders the recombination process of electron-hole pairs and thus improves the efficiency of interfacial charge separation. In

RSC Advances Accepted Manuscript

addition, the photogenerated electrons in the CB of Fe_2O_3 can reduce the dissolved O_2 to yield abundant active $\cdot O_2^-$, together with the holes in the VB of g-C_3N_4 employed for further effective oxidation of RhB. Therefore, owing to the high transfer and separation efficiency of charge carriers in this heterojunction system, Fe_2O_3/g-C_3N_4 composites demonstrate superior photocatalytic performance compared with that of pure g-C_3N_4 and Fe_2O_3.

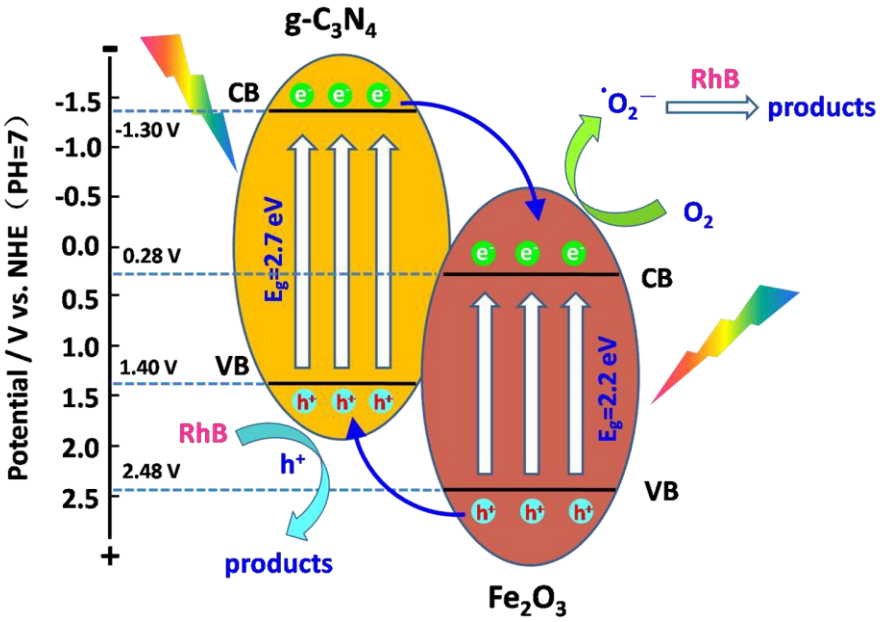

Fig. 10 Proposed mechanism for the photocatalytic degradation of RhB over Fe_2O_3/g-C_3N_4 nanocomposites under visible light irradiation.

4. Conclusions

In summary, we have successfully fabricated an efficient visible-light photocatalyst for RhB degradation by loading a small amount of Fe_2O_3 onto the g-C_3N_4 nanosheets through a facile deposition-precipitation method. The crystal structure, morphology, element chemical states and optical absorption of the composites have been investigated, and the results confirm the strong interaction and the formation of heterojunction structure between highly dispersed Fe_2O_3 nanocrystals and g-C_3N_4 nanosheets. Photocatalytic RhB degradation results demonstrate that introducing of Fe_2O_3 nanoparticles brought about significant improvement of photocatalytic activity of g-C_3N_4 and that the optimum photocatalytic activity of Fe_2O_3/g-C_3N_4 composites with a weight ratio of 0.1% Fe_2O_3 is much higher than that of pure g-C_3N_4 and Fe_2O_3 under visible light irradiation. Radical trapping experiments indicate that

RSC Advances Accepted Manuscript

both holes and superoxide radicals are the main oxidative species for RhB photodegradaion. A possible photocatalytic mechanism is proposed based on the experimental results. The accelerated photoinduced electron-hole transfer and separation, decreased recombination rate and band energy matching lead to the enhancement of photocatalytic performance for Fe_2O_3/g-C_3N_4 heterojunction. This work provides a promising approach for developing an efficient composite heterojunction photocatalyst by tuning and control of dispersion and contact between different components for visible-light-driven photocatalytic reaction.

Acknowledgements

This work was financially supported by National Natural Science Foundation of China (No. 21503100) and Natural Science Foundation of Jiangxi Province of China (No. 20151BAB213010). Ailing Jin was supported by the Scientific Research Foundation of Graduate School of Jiangxi Province (YC2015-S123).

Electronic Supplementary Information (ESI) Available: XRD pattern of 20 wt% Fe_2O_3/g-C_3N_4 nanocomposite and nitrogen adsorption/desorption isotherm of pure g-C_3N_4.

Notes and references

1 A. Kudo and Y. Miseki, *Chem. Soc. Rev.*, 2009, **38**, 253.

2 X. Chen, S. Shen, L. Guo and S. S. Mao, *Chem. Rev.*, 2010, **110**, 6503.

3 M. Pelaez, N. T. Nolan, S. C. Pillai, M. K. Seery, P. Falaras, A. G. Kontos, P. S. M. Dunlop, J. W. J. Hamilton, J. A. Byrne, K. O'Shea, M. H. Entezari and D. D. Dionysiou, *Appl. Catal., B*, 2012, **125**, 331.

4 S. N. Habisreutinger, L. Schmidt-Mende and J. K. Stolarczyk, *Angew. Chem. Int. Ed.*, 2013, **52**, 7372.

5 X. Lang, X. Chen and J. Zhao, *Chem. Soc. Rev.*, 2014, **43**, 473.

6 Z. Zhao, Y. Sun, F. Dong, Y. Zhang and H. Zhao, *RSC Adv.*, 2015, **5**, 39549.

7 M. R. Gholipour, D. Cao-Thang, F. Beland and D. Trong-On, *Nanoscale*, 2015, **7**, 8187.

8 Y. Qu and X. Duan, *Chem. Soc. Rev.*, 2013, **42**, 2568.

9 X. Wang, K. Maeda, A. Thomas, K. Takanabe, G. Xin, J. M. Carlsson, K. Domen and M.

RSC Advances Accepted Manuscript

Antonietti, *Nat. Mater.*, 2009, **8**, 76.

10 X. Wang, S. Blechert and M. Antonietti, *ACS Catal.*, 2012, **2**, 1596.

11 S. Cao, J. Low, J. Yu and M. Jaroniec, *Adv. Mater.*, 2015, **27**, 2150.

12 J. Zhang, B. Wang and X. Wang, *Prog. Chem.*, 2014, **26**, 19.

13 J. Zhu, P. Xiao, H. Li and S. A. C. Carabineiro, *ACS Appl. Mater. Interfaces*, 2014, **6**, 16449.

14 S. Hu, L. Ma, J. You, F. Li, Z. Fan, G. Lu, D. Liu and J. Gui, *Appl. Surf. Sci.*, 2014, **311**, 164.

15 S. Zhang, J. Li, M. Zeng, J. Li, J. Xu and X. Wang, *Chem. —Eur. J.*, 2014, **20**, 9805.

16 K. Wang, Q. Li, B. Liu, B. Cheng, W. Ho and J. Yu, *Appl. Catal., B*, 2015, **176**, 44.

17 S. Hu, R. Jin, G. Lu, D. Liu and J. Gui, *RSC Adv.*, 2014, **4**, 24863.

18 J. Zhang, F. Guo and X. Wang, *Adv. Funct. Mater.*, 2013, **23**, 3008.

19 J. Sun, J. Zhang, M. Zhang, M. Antonietti, X. Fu and X. Wang, *Nat. Commun.*, 2012, **3**.

20 D. Chen, K. Wang, W. Hong, R. Zong, W. Yao and Y. Zhu, *Appl. Catal., B*, 2015, **166**, 366.

21 S. Min and G. Lu, *J. Phys. Chem. C*, 2012, **116**, 19644.

22 Y. He, Y. Wang, L. Zhang, B. Teng and M. Fan, *Appl. Catal., B*, 2015, **168**, 1.

23 Y. He, L. Zhang, M. Fan, X. Wang, M. L. Walbridge, Q. Nong, Y. Wu and L. Zhao, *Sol. Energy Mater. Sol. Cells*, 2015, **137**, 175.

24 Z. Tong, D. Yang, T. Xiao, Y. Tian and Z. Jiang, *Chem. Eng. J.*, 2015, **260**, 117.

25 S. Ye, L.-G. Qiu, Y.-P. Yuan, Y.-J. Zhu, J. Xia and J.-F. Zhu, *J. Mater. Chem. A*, 2013, **1**, 3008.

26 J. Theerthagiri, R. A. Senthil, A. Priya, J. Madhavan, R. J. V. Michael and M. Ashokkumar, *RSC Adv.*, 2014, **4**, 38222.

27 Y. Liu, Y.-X. Yu and W.-D. Zhang, *Int. J. Hydrogen Energy*, 2014, **39**, 9105.

28 L. Ge, F. Zuo, J. Liu, Q. Ma, C. Wang, D. Sun, L. Bartels and P. Feng, *J. Phys. Chem. C*, 2012, **116**, 13708.

29 L. Huang, H. Xu, Y. Li, H. Li, X. Cheng, J. Xia, Y. Xu and G. Cai, *Dalton Trans.*, 2013, **42**, 8606.

30 M. Mishra and D.-M. Chun, *Appl. Catal., A*, 2015, **498**, 126.

RSC Advances Accepted Manuscript

31 S. Yang, Y. Xu, Y. Sun, G. Zhang and D. Gao, *CrystEngComm*, 2012, **14**, 7915.

32 S. K. Apte, S. D. Naik, R. S. Sonawane and B. B. Kale, *J. Am. Ceram. Soc.*, 2007, **90**, 412.

33 T. Li, L. Zhao, Y. He, J. Cai, M. Luo and J. Lin, *Appl. Catal., B*, 2013, **129**, 255.

34 S.-W. Cao, X.-F. Liu, Y.-P. Yuan, Z.-Y. Zhang, Y.-S. Liao, J. Fang, S. C. J. Loo, T. C. Sum and C. Xue, *Appl. Catal., B*, 2014, **147**, 940.

35 Z. Zhang, J. Huang, M. Zhang, L. Yuan and B. Dong, *Appl. Catal., B*, 2015, **163**, 298.

36 D. J. Martin, K. Qiu, S. A. Shevlin, A. D. Handoko, X. Chen, Z. Guo and J. Tang, *Angew. Chem. Int. Ed.*, 2014, **53**, 9240.

37 S. Kumar, S. Tonda, A. Baruah, B. Kumar and V. Shanker, *Dalton Trans.*, 2014, **43**, 16105.

38 K. Volgmann, F. Voigts and W. Maus-Friedrichs, *Surf. Sci.*, 2010, **604**, 906.

39 H. Y. Lin, Y. W. Chen and W. J. Wang, *J. Nanopart. Res.*, 2005, **7**, 249.

40 Y. Tian, B. Chang, Z. Yang, B. Zhou, F. Xi and X. Dong, *RSC Adv.*, 2014, **4**, 4187.

41 S. C. Yan, Z. S. Li and Z. G. Zou, *Langmuir*, 2010, **26**, 3894.

42 Y.-S. Xu and W.-D. Zhang, *ChemCatChem*, 2013, **5**, 2343.

43 L. Ge, C. Han and J. Liu, *J. Mater. Chem.*, 2012, **22**, 11843.

44 S. B. Rawal, S. Bera, D. Lee, D.-J. Jang and W. I. Lee, *Catal. Sci. Technol.*, 2013, **3**, 1822.

45 S. Chu, Y. Wang, Y. Guo, J. Feng, C. Wang, W. Luo, X. Fan and Z. Zou, *ACS Catal.*, 2013, **3**, 912.

46 Y. Cui, Z. Ding, P. Liu, M. Antonietti, X. Fu and X. Wang, *Phys. Chem. Chem. Phys.*, 2012, **14**, 1455.

RSC Advances Accepted Manuscript